JOURNAL OF COMPUTATIONAL PHYSICS 90, 396–430 (1990)

Numerical Simulation of Unsteady Viscous Free Surface Flow

BALASUBRAMANIAM RAMASWAMY

Department of Mechanical Engineering and Materials Science, Rice University, Houston, Texas 77251-1892

Received September 6, 1988; revised June 7, 1989

A finite element method is presented for the numerical simulation of time-dependent incompressible viscous free surface flows. The time-dependent primitive equations are solved sequentially using explicit time marching procedure. The method is based on a velocity correction approach to the time integration of the Navier–Stokes equations in which only the incompressibility condition is treated implicitly. A special arbitrary mixed Lagrangian–Eulerian description has been used to avoid the typical problems encountered in a purely Lagrangian description. The method appears applicable for small computers; problems requiring several thousand nodes can be solved on personal computers. Numerical experiments have been performed that show that this approach is reasonably efficient and robust for a range of complicated highly nonlinear problems. © 1990 Academic Press, Inc.

1. INTRODUCTION

The mathematical study of the motion of waves dates back as far as the works of Lagrange, around 1800. Since then, steady progress has been made in this field by many researchers through the application of mathematical physics. Two important approximate theories have evolved: the linear theory for small amplitude waves and the non-linear for waves in shallow depths. Some progress has even been made in the solution of the general nonlinear problems by the use of perturbation theory. However, the application of analytical techniques to these problems has been hindered by the difficulties of non-linearities, not the least of which is the fact that the flow domain is not known *a priori* but is part of the solution. The advent of numerical methods was therefore accompanied by a renewed interest in previously intractible problems. Earlier classical approaches were then largely used to confirm the validity of a numerical procedure prior, to its application to complex problems.

Fluid flow is generally described using one of the following viewpoints: (1) Eulerian: Attention is focused on some point in space and the changes in the fluid can be described as functions of time at this point. (2) Lagrangian: Attention is focused on an infinitesimal fluid element and the changes in this fluid element can be expressed as functions of time. Major analytical works in fluid dynamics use one

0021-9991/90 $3.00

or both of these viewpoints; correspondingly numerical techniques have developed along these lines.

The early papers on finite element techniques for free surface fluid flow problems [1–10] used the Eulerian viewpoint to describe fluid flow; that is, instead of considering the fluid at all spatial points, attention is focused on a finite number of fixed points. Eulerian numerical techniques are characterized by finding the values of the fluid variables at the mesh points of a fixed grid. The Eulerian method has several advantages. The fluid can undergo arbitrarily great distortions without loss of accuracy, and outflow walls are particularly easy to handle. However, local resolution is difficult to achieve, and interfaces become blurred. Moreover, one must generate new finite element discretizations to pursue the profile of the free surface, which requires a lot of computational time.

Later, Lagrangian finite element techniques [11–13] were developed for free surface problems. Instead of considering every infinitesimal fluid element, researchers focused their attention on a finite number of these elements, the fluid was conveniently represented by an array of particles. The fluid properties such as density, pressure, and velocity are then localized to a finite number of particles that move with the fluid. Lagrangian methods permit accurate treatment of relatively low-amplitude free surface motions. In addition, they are very easy to modify for multimaterial studies and the incorporation of surface-tension effects. Their principal disadvantage is that accuracy breaks down when distortions are large.

To overcome the above-mentioned difficulties in both Eulerian and Lagrangian approaches, techniques have been proposed in this paper wherein the nodal points of the mesh can be displayed independently of the fluid motion. The approach, a mixed Lagrangian–Eulerian method, combines Lagrangian and Eulerian computing methods for fluid flow based on Hirt's [14] findings regarding the finite difference method. Because of the Lagrangian aspects of this technique, it is applicable to free surface flows, but it also retains the ability of Eulerian techniques to overcome undesirable grid distorsions often associated with Lagrangian methods. The basic hydrodynamic part of each cycle of the mixed method described in this paper is divided into two phases. The first phase is a typical Lagrangian calculation. In the second phase, the rezone velocities are specified to reduce distortions in the fluid domain and perform all the convective flux calculations, which must be included if the mesh is not a purely Lagrangian. In practical applications, the hydrodynamics problem would be run for a while with the pure Lagrangian code and then be stopped when the mesh becomes somewhat distorted. The rezone code would then be implemented to smooth out the mesh, so that a desirable mesh configuration can be maintained. It should be noted that no time change occurs during the rezoning operation. The mesh would then be passed back to the hydrodynamics code for more time-dependent calculations. By this infrequent use of rezoning, we hope that the mesh distortions may be held down enough to permit the problem to run satisfactorily.

2. Governing Equations in the ALE Description

The arbitrary Lagrangian–Eulerian (ALE) formulation introduces a reference configuration as shown in Fig. 1, which consists of a set of grid points in arbitrary motion in space. Each point of this reference configuration may be identified by an invariant set of two independent coordinates χ_i. The motion of the reference frame then be expressed as an arbitrary continuous function of χ and the time t:

$$x_i = x_i(\chi_j, t). \tag{1}$$

The formulation requires an inverse to Eq. (1) to exist; i.e.,

$$\chi_i = \chi_i(x_j, t) \tag{2}$$

such that the Jacobian $J = \det|\partial x_i/\partial \chi_j|$ is non-vanishing. The above description of the referential system does not refer directly to the motion of the particles constituting the continuum; therefore it is necessary to establish a correlation between this system and the Lagrangian system that inherently defines the motion of the particles. Such a relation demands a unique connection between the two systems at every stage of deformation of the continuum; i.e., a single material point may coincide with only one point of the grid system (though not necessarily always the same point). In the Lagrangian system the material particles are identified by a set of coordinates X_i known as material coordinates. In the deformed configuration the material particle may occupy a position x_i, which may be expressed in terms of the material coordinates and time t as

$$x_i = x_i(X_j, t), \tag{3}$$

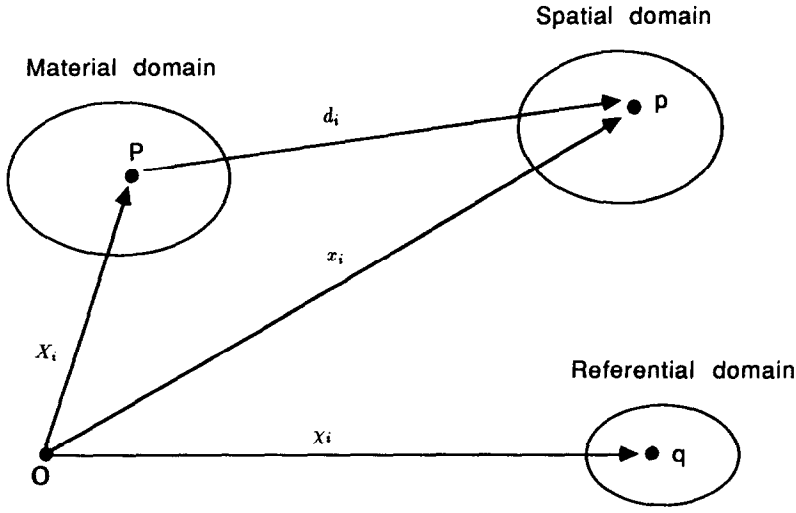

FIG. 1. Coordinate system for ALE representation.

where the inverse of Eq. (3) is assumed to exist such that the determinant of the Jacobian $\hat{J} = \det|\partial x_i/\partial X_j|$ is not equal to zero. To obtain a relation between the referential and material coordinates, we assume a point x_i in space occupied at time t by elements of both the systems (i.e., material point and grid point). Thus, by virtue of the existence of the inverse mappings of (2) and (3), an interrelation between the motion of material and referential (grid) points may be established as

$$\chi_i = f_i(x_j, t) = \hat{f}_i(X_k, t). \tag{4}$$

Equation (4) may be interpreted as a mapping of the material domain onto the referential domain. With the notion that such a relation exists, we can then derive the conservation of equations of mechanics with respect to a referential configuration. The Reynolds transport theorem is applied to an arbitrary control volume moving through a deforming continuum that is then shrunk to a point. This yields the resulting field equations in the ALE description as

Continuity.

$$\left.\frac{\partial(J\rho)}{\partial t}\right|_{\chi_i} + J(\rho(u_i - w_i))_{,j} = 0, \qquad \text{in } V. \tag{5}$$

For incompressible fluids, Eq. (5) reduces to

$$u_{i,i} = 0, \qquad \text{in } V. \tag{6}$$

Momentum.

$$\frac{\partial u_i}{\partial t} + (u_j - w_j)\, u_{i,j} + \frac{1}{\rho}\, p_{,i} - \nu(u_{i,j} + u_{j,i})_{,j} - f_i = 0, \qquad \text{in } V, \tag{7}$$

where ρ refers to the material density, f_i is the body force, and p is the pressure. In the above equations w_i $(=(\partial x_i/\partial t)|_{\chi_i})$ represents the velocity of a representative grid point and u_i $(=(\partial x_i/\partial t)|_{X_i})$ represents the velocity of a material point coinciding with the grid point at time t.

Equations (6) and (7) may be interpreted as material conservation laws with respect to arbitrary moving grid points. One advantage of the ALE description is that, in general, the velocity w_i of the reference frame (i.e., representative grid point) may not be the same as the coincident material point velocity u_i, as in the Lagrangian description, or it may be zero, as in the Eulerian description. In the event that a grid point may coincide with a material point, the relative velocity term $(w_i - u_i)$ becomes zero, resulting in the vanishing of the convective terms, and consequently the set of equations becomes Lagrangian. Similarly, a pure Eulerian description is obtained by simple setting $w_i = 0$. It is this flexibility to use a different pointwise description, where the grid points may be made to move with the material or remain stationary in space or even to move with any arbitrary velocity, that makes the ALE description so attractive. This feature provides greater scope

for the user to maneuver the nodal or grid points effectively in a large deformation analysis.

The boundary conditions and initial conditions for the ALE formulation are identical to that for Eulerian and Lagrangian methods. The boundary S consists of two kinds of boundaries, namely, the free surface boundary S_1 and the solid wall boundary S_2 of the tank. On the free surface boundary, the normal stress should be equal to the atmospheric pressure and the tangential stress should vanish. To express these conditions in differential form, we need the stress tensor for an incompressible fluid, which is given by

$$\sigma_{ij} = -p\delta_{ij} + \mu(u_{i,j} + u_{j,i}). \tag{8}$$

Physically, $-\sigma_{ij}$ is the amount of the ith-component of momentum flowing per unit time through a unit area normal to the jth direction. Since there is no flux of momentum through a free surface, the boundary condition is

$$\sigma_{ij} \cdot n_j = 0, \qquad \text{on } S_1, \tag{9}$$

where the atmospheric pressure is assumed to be zero and n_j is the direction cosine of the outward normal on the boundary with respect to the x_j axis. On the solid wall, the velocity boundary condition in discrete form is specified as

$$u_i = \hat{u}_i, \qquad \text{on } S_2, \tag{10}$$

where $\hat{u}_i$ denotes the function that is given on the boundary.

In the case of a free fluid boundary, the time evolution of the height function is governed by a kinematic equation expressing the fact that the surface must move with the fluid:

$$\frac{\partial \eta}{\partial t} + (u_i^{(s)} - w_i^{(s)})\, \eta_{,i} = 0, \tag{11}$$

where η is the surface elevation measured from the fundamental fluid level and $u_i^{(s)}$ and $w_i^{(s)}$ are the x_i-components of the fluid particle velocity and mesh velocity at nodal points of the free surface.

The initial conditions for the Navier–Stokes problem consist of specifying the value of velocity at the initial time,

$$u_i(x_i, 0) = u_i^{(0)}(x_i), \tag{12}$$

with the initial velocity, $u_i^{(0)}(x_i)$, satisfying the incompressibility condition,

$$u_{i,i}^{(0)} = 0, \tag{13}$$

and

$$u_i(x_i, 0)\, n_i = \hat{u}_i(x_i, 0)\, n_i, \qquad \text{on } S_2. \tag{14}$$

3. Time Discretization

An interesting computational scheme based on explicit time integration and valid for incompressible flows can be obtained from the ideas developed in finite difference methods. In deriving such a scheme, we note that the convective terms in Eq. (7) vanish in the Lagrangian formulation—that is, when $u_i = w_i$. It is this reduction that leads us to first solve the Lagrangian integral equations in the first step of the calculational cycle, phase I, and then to add the convective contributions as a separate step in phase II. In phases I and II we also have an implicit pressure calculation that permits solutions to satisfy the incompressibility constraint condition. Let u_i^n and p^n be the velocity and pressure fields at time t^n, where $t^n = t^{n-1} + \Delta t$. From u_i^n, p^n, and the boundary specifications, the fields u_i^{n+1} and p^{n+1} are calculated as described below.

3.1. *Phase I Lagrangian Calculations*

Basic Concepts of the Lagrangian Method

In Lagrangian formulation, it is necessary to discretize time and fluid material. This is in contrast to a numerical solution of an Eulerian formulation, where one would discretize time and space. The basic concept of the analysis presented here is that the matrial time derivative can be determined approximately by the functions known at both deformed and undeformed positions during a short time increment. The function at the deformed position cannot be obtained before computation. Thus, an iterative computation is necessary. Assuming the total time interval is divided into many short time increments, denoted by Δt, and we discretize the fluid into many triangular finite elements. The material acceleration is then the time derivative considering the change of location of a fluid particle. In this phase, the material acceleration can be approximated by the increment of the velocity in the following form:

$$\left.\frac{\partial u_i}{\partial t}\right|_{x_i} = \frac{(u_i^L - u_i^n)}{\Delta t}. \tag{15}$$

In this formulation, the coordinates x_i appears as dependent variables, and the independent variables instead become fluid particle labels, which are conveniently defined by the initial location of the fluid particles x_i^0 at reference time t_0. The coordinates, when viewed as functions of particles and time, are then expressed as the displacement functions $x_i = x_i(x_i^0, t_0, t)$, where $x_i^0 = (x_1^0, x_2^0)$. If the fluid particle is defined as $P_k = P_k(x_i^0, t_0)$, then the velocity components, pressure field, and positions of each fluid particle $P_k = P_k(x_i^0, t_0)$, with the initial location x_i^0 at time t_0 are defined by

$$u_i^n = u_i(P_k, t^n) \tag{16}$$

$$p^n = p(P_k, t^n) \tag{17}$$

$$x_i^n = x_i(P_k, t^n) \tag{18}$$

and

$$u_i^L = u_i(P_k, t^{n+1}) \tag{19}$$

$$p^L = p(P_k, t^{n+1}) \tag{20}$$

$$x_i^L = x_i(P_k, t^{n+1}). \tag{21}$$

The location of a nodal point after the time increment Δt is given by

$$x_i(P_k, t^{n+1}) \equiv x_i^L \approx x_i^n + \frac{\Delta t}{2}(u_i^L + u_i^n). \tag{22}$$

Since the location of a particle x_i^L is a function of u_i^L, which is not known *a priori*, the finite element analysis based on Eq. (22) must be solved by some iterative procedure that must be repeated in every time step. The algorithm for an iterative process is briefly explained below.

At the initial step of iteration, velocity $u_i^{L(0)}$, pressure $p^{L(0)}$, and position $x_i^{L(0)}$ are computed as

$$\tilde{u}_i^{L(0)} = \tilde{g}_i(u_i^n, f_i^n, x_i^n) \tag{23}$$

$$p^{L(0)} = h(\tilde{u}_i^{L(0)}, x_i^n) \tag{24}$$

$$u_i^{L(0)} = g_i(\tilde{u}_i^{L(0)}, p^{L(0)}, x_i^n) \tag{25}$$

$$x_i^{L(0)} = x_i^n + \Delta t u_i^n, \tag{26}$$

where $\tilde{u}_i^{L(0)}$ and $u_i^{L(0)}$, for example, are the values of the intermediate and final velocity components at the initial step of iteration in the $(n+1)$th time interval; g_i and h mean that velocity and pressure can be computed following the velocity correction method based on the previously known velocity u_i^n and body forces f_i^n at position x_i^n and at time t^n. At the mth iteration cycle (where $m = 1, 2, ..., MAX$; MAX is the maximum number of iterations), the values are updated by the following equations:

$$\tilde{u}_i^{L(m)} = \tilde{g}_i(u_i^n, f_i^n, x_i^{L(m-1)}) \tag{27}$$

$$p^{L(m)} = h(\tilde{u}_i^{L(m)}, x_i^{L(m-1)}) \tag{28}$$

$$u_i^{L(m)} = g_i(\tilde{u}_i^{L(m)}, p^{L(m)}, x_i^{L(m-1)}) \tag{29}$$

$$x_i^{L(m)} = x_i^n + \frac{\Delta t}{2}(u_i^{L(m)} + u_i^n). \tag{30}$$

Equations (28) and (29) specify that the velocity and pressure can be computed using the latest positions of the fluid particles. The iteration is repeated until the computed velocity satisfies the convergence criterion

$$|u_i^{L(m)} - u_i^{L(m-1)}| < \varepsilon, \tag{31}$$

where ε is a previously defined small value. If the process converges then the values obtained at the mth iteration are assigned to $(n+1)$th time step. Thus, the velocity and pressure considering the change of position of a fluid particle can be computed. The computation is repeated for all $n = 1, 2, ..., NMAX$, where $NMAX$ is the total number of time points.

Velocity Correction Method

To obtain the velocity and pressure at time t^{n+1}, we successfully use the velocity correction method in the present analysis. This subsection describes how to compute g_i and h in Eqs. (25) and (24), which in turn help to compute u_i^L and p^L in Eqs. (29) and (28).

At first, an intermediate velocity field $\tilde{u}_i^L$ that does not satisfy the incompressibility constraint is derived from a time-discretized version of the momentum equation in which the pressure terms are omitted. Then, the field $\tilde{u}_i^L$ is decomposed into the sum of a vector field with zero divergence and a vector field with zero curl. The divergenceless component is the end-of-step Lagrangian velocity vectors u_i^L, whereas the irrotational one is related to the gradient of the pressure field p^L.

The intermediate Lagrangian nodal velocity fields $\tilde{u}_i^L$ not satisfying the incompressibility condition is derived from the previous cycle's velocity vectors, position vectors, and body forces by employing a purely explicit Euler's first-order scheme:

$$\tilde{u}_i^L = u_i^n + \Delta t\{\nu(u_{i,j}^n + u_{j,i}^n)_{,j} + f_i^n\} \tag{32}$$

$$\tilde{u}_i^L = \hat{u}_i, \qquad \text{on } S_2. \tag{33}$$

Once the intermediate velocity has been computed, the end-of-step velocity u_i^L is obtained by adding the dynamical effect of the still unknown pressure p^L, which is to be determined so that the incompressibility condition remains satisfied to $\tilde{u}_i^L$:

$$u_i^L = \tilde{u}_i^L - \Delta t p_{,i}^L. \tag{34}$$

Taking divergence on both sides of Eq. (34) together with incompressibility constraint $u_{i,i}^L = 0$, the following equation for pressure can be derived:

$$p_{,ii}^L = \frac{1}{\Delta t}\tilde{u}_{i,i}^L. \tag{35}$$

The concomitant boundary conditions on p for use in the first of Eq. (35) are derived from Eq. (34) together with the incompressibility constraint and are either Neumann or Dirichlet boundary conditions, i.e., prescribed normal derivative, $\partial p/\partial n = n \cdot (\tilde{u}_i^L - u_i^L)$ or prescribed p which can be obtained by integrating the prescribed tangential velocities from $\partial p/\partial \tau = \tau \cdot (\tilde{u}_i^L - u_i^L)$ over the boundary.

Once the pressure has been determined from Eq. (35), Lagrangian nodal velocities are calculated from Eq. (34). This overall iterative solution method is illustrated in Fig. 2. Unlike most previous finite element methods, the current

$$\left.\frac{Du_i}{Dt}\right|_{X_i} = \frac{(u_i^L - u_i^n)}{\Delta t}$$

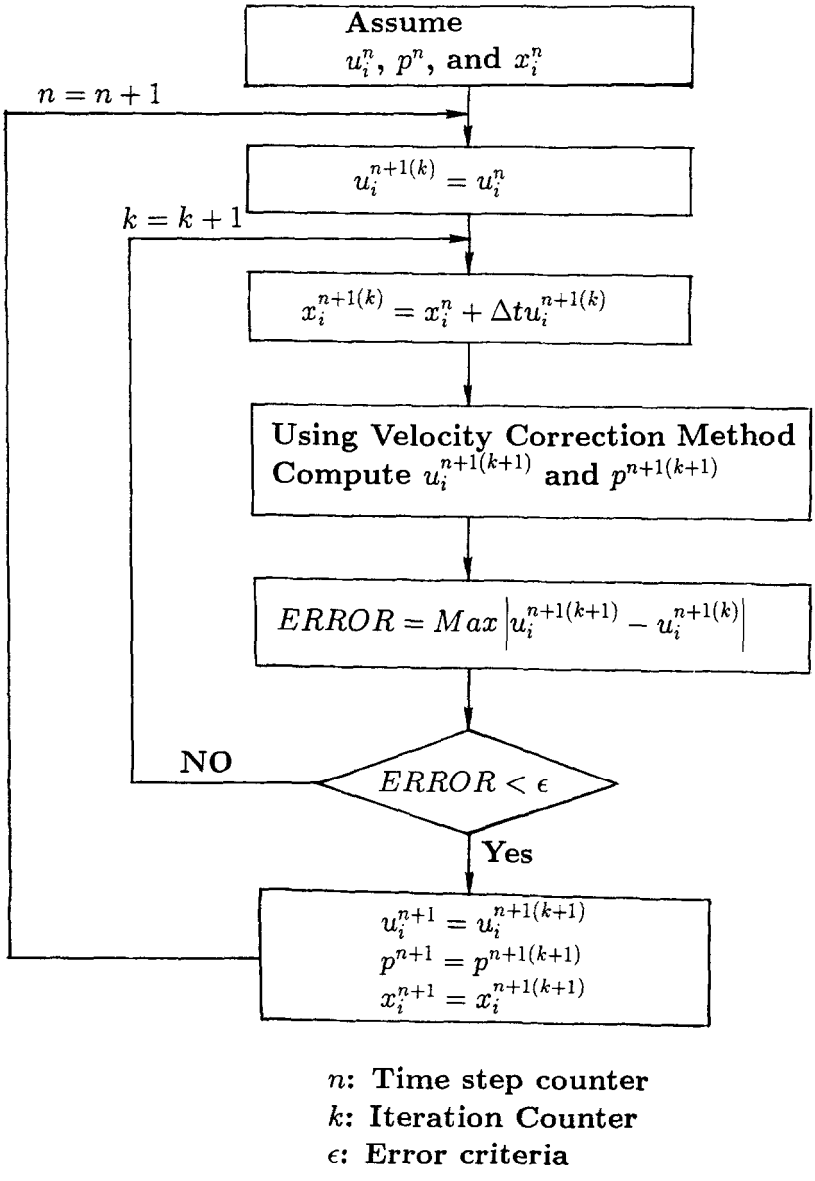

FIG. 2. Flowchart for the global Lagrangian algorithm.

formulation uses a segregated solution approach; i.e., the velocities and pressure are solved for in a sequential manner rather than simultaneously. The use of a segregated solution results in a considerable savings of storage and execution time and allows for problems of practical size to be treated. If only a Lagrangian calculation is wanted, then vertices are moved according to Eq. (22), and the phase I calculation can be repeated for more time-dependent calculations. Otherwise, rezone velocities must be specified, and phase II calculations must be performed.

3.2. *Phase II Rezone or Convective Flux Calculation*

In phase I, the contribution from the convective terms in Eqs. (32)–(34) were not evaluated. In Phase II, we now add the contributions from these terms to the time-advanced level L values.

All the examples treated in this paper are two-dimensional. Since we know the shape of the free surface and the solid boundary of the tank or container, it is easy to distribute the grid points in both horizontal and vertical directions equally. Once the new location of the grid points is known, the mesh velocity can be calculated:

$$w_i = \frac{x_i^{n+1} - x_i^L}{\Delta t}. \tag{36}$$

There are two types of quantities to be updated in the rezoning: (1) element quantities, namely, the mass or volume; and (2) vertex quantities, namely, the velocity components u_i and the pressure field p. Using Eq. (36) we can now compute new element volumes and masses. The calculations that account for the transfer of mass and momentum between elements during rezoning now remain to be described. A temporary velocity field that accounts for the convective fluxes is first calculated,

$$\tilde{u}_i^{n+1} = \tilde{u}_i^L - \Delta t(w_j - u_j^L)\, u_{i,j}^n, \tag{37}$$

with

$$\tilde{u}_i^{n+1} = \hat{u}_i, \qquad \text{on } S_2. \tag{38}$$

Final velocities for the cycle are obtained by combining the temporary velocities $\tilde{u}_i^{n+1}$ with the pressure acceleration in the following manner:

$$u_i^{n+1} = \tilde{u}_i^{n+1} - \Delta t p_{,i}^{n+1}. \tag{39}$$

The pressure needed in Eq. (39) are those that ensure satisfaction of the incompressibility condition. That is, the final velocity field must possess a zero velocity divergence in every element. This is accomplished by solving the equation that governs the pressure field:

$$p_{,ii}^{n+1} = \frac{1}{\Delta t} \tilde{u}_{i,i}^{n+1}. \tag{40}$$

The preceding equation (40) is a symmetric system of linear algebraic equations that may be solved via a direct method such as the skyline version of Gaussian elimination. Once the pressure has been obtained, the end-of-step velocity is computed from Eq. (39). The position of the free surface is calculated from the following equation:

$$\eta^{n+1} = \eta^n + \Delta t(w_i^{(s)} - u_i^{L(s)})\,\eta^n_{,i}. \tag{41}$$

This completes the steps contained in a cycle of the solution technique.

4. Finite Element Method

In the above, the explanation of the algorithm was given in a continuum space. In the finite element method, the variables u_i, p, and η are discretized by the following finite element approximations,

$$u_i = \Phi_\alpha u_{\alpha i} \tag{42}$$

$$p = \Phi_\alpha p_\alpha \tag{43}$$

$$\eta = \Phi_\alpha \eta_\alpha, \tag{44}$$

where Φ_α is the interpolation function, $u_{\alpha i}$ denotes the nodal value of velocity at the αth node of the finite element in the ith direction, and p_α indicates the nodal value of pressure at the αth node. In the present study, the most simple three-node triangular element is used. Using the conventional Galerkin–Bubnov finite element method, we discretize Eqs. (32), (34), (35), (37), (39), and (40) in space and reduce them to the following semi-discrete version of the weak form:

For Phase I.

$$\bar{M}^L_{\alpha\beta}\tilde{u}^L_{\beta i} = \bar{M}^n_{\alpha\beta}u^n_{\beta i} - \Delta t(S^n_{\alpha i\beta j}u^n_{\beta j} - N^n_\alpha f^n_{\alpha i} - \hat{\Omega}^n_{\alpha i}) \tag{45}$$

$$\bar{M}^L_{\alpha\beta}u^L_{\beta i} = \bar{M}^L_{\alpha\beta}\tilde{u}^L_{\beta i} - \Delta t H^L_{\alpha i\beta}\,p^L_\beta \tag{46}$$

$$A^L_{\alpha\beta}\,p^L_\beta = -\frac{1}{\Delta t}H^L_{\alpha i\beta}\tilde{u}^L_{\beta i} + \hat{\Sigma}^L_\alpha. \tag{47}$$

For Phase II.

$$\bar{M}^{n+1}_{\alpha\beta}\tilde{u}^{n+1}_{\beta i} = \bar{M}^L_{\alpha\beta}\tilde{u}^L_{\beta i} + \Delta t K^n_{\alpha\beta\gamma j}(w_{\beta j} - u^n_{\beta j})\,u^n_{\gamma i} \tag{48}$$

$$\bar{M}^{n+1}_{\alpha\beta}u^{n+1}_{\beta i} = \bar{M}^{n+1}_{\alpha\beta}\tilde{u}^{n+1}_{\beta i} - \Delta t H^{n+1}_{\alpha i\beta}p^{n+1}_\beta \tag{49}$$

$$A^{n+1}_{\alpha\beta}p^{n+1}_\beta = -\frac{1}{\Delta t}H^{n+1}_{\alpha i\beta}\tilde{u}^{n+1}_{\beta i} + \hat{\Sigma}^{n+1}_\alpha \tag{50}$$

$$\bar{M}^{n+1}_{\alpha\beta}\eta^{n+1}_\beta = \bar{M}^n_{\alpha\beta}\eta^n_\beta + \Delta t K^n_{\alpha\beta\gamma j}(w_{\beta j} - u^n_{\beta j})\,\eta^n_\gamma, \tag{51}$$

where $M_{\alpha\beta}$, $K_{\alpha\beta\gamma j}$, $S_{\alpha i\beta j}$, $H_{\alpha i\beta}$, and $A_{\alpha\beta}$ are mass, convection, diffusion, pressure gradient, and Laplacian matrices, respectively. In Eqs. (45)–(51), $\bar{M}_{\alpha\beta}$ is the lumped mass matrix obtained simply by summing across each row of the consistent mass matrix $M_{\alpha\beta}$ and placing the results in the diagonal.

5. Numerical Examples

5.1. *Free Oscillation*

The free oscillation of a liquid with a small amplitude is computed to verify the present formulation. The water column is 1.0 units wide and 1.0 units high, as shown in Fig. 3. Gravity acts downward with a unit magnitude. As the initial profile of the free surface, the first antisymmetric natural mode is assumed as

$$\eta(x_1, 0) = a \sin\left(\frac{\pi}{2b} x_1\right), \tag{52}$$

where a is the amplitude of the antisymmetric natural mode, which is assumed to 0.01 units, and $2b$ is the width of the container. The free slip boundary condition is specified on the solid boundary of the tank. Figure 3b shows the computed time histories of $\eta(\pm\frac{1}{2}, t)$ in the non-viscous case. From the computed results it can be seen that the free surface oscillates at a nearly constant amplitude without any artificial damping effect. Figure 3c shows the time histories $\eta(\pm\frac{1}{2}, t)$ with a viscous effect, where $\nu = 0.01$. The computed results are remarkably good and provide a nice check on mass and momentum conservation.

5.2. *Nonlinear Oscillation*

This example has been chosen to demonstrate the validity of the present computing technique with a highly non-linear effect. Fluid initially at rest in a rectangular tank is impulsively set into oscillation by a cosine pressure pulse applied at the free surface. The linear analysis for the change in surface elevation, η, above the initially undisturbed free surface height D, gives

$$\eta = -A \sqrt{\left(\frac{\zeta}{gD}\right)} \sin\left[t \sqrt{\left(\frac{g\zeta}{D}\right)}\right] \cos(kx_1), \tag{53}$$

where

$$\zeta = kD \tanh(kD). \tag{54}$$

Here $k = 2\pi/\lambda$, where λ is the disturbance wavelength, and g is the acceleration of gravity. The initial pressure pulse on the free surface is described by

$$p(t) = A\delta(t) \cos(kx_1), \tag{55}$$

where $\delta(t)$ is the dirac delta function.

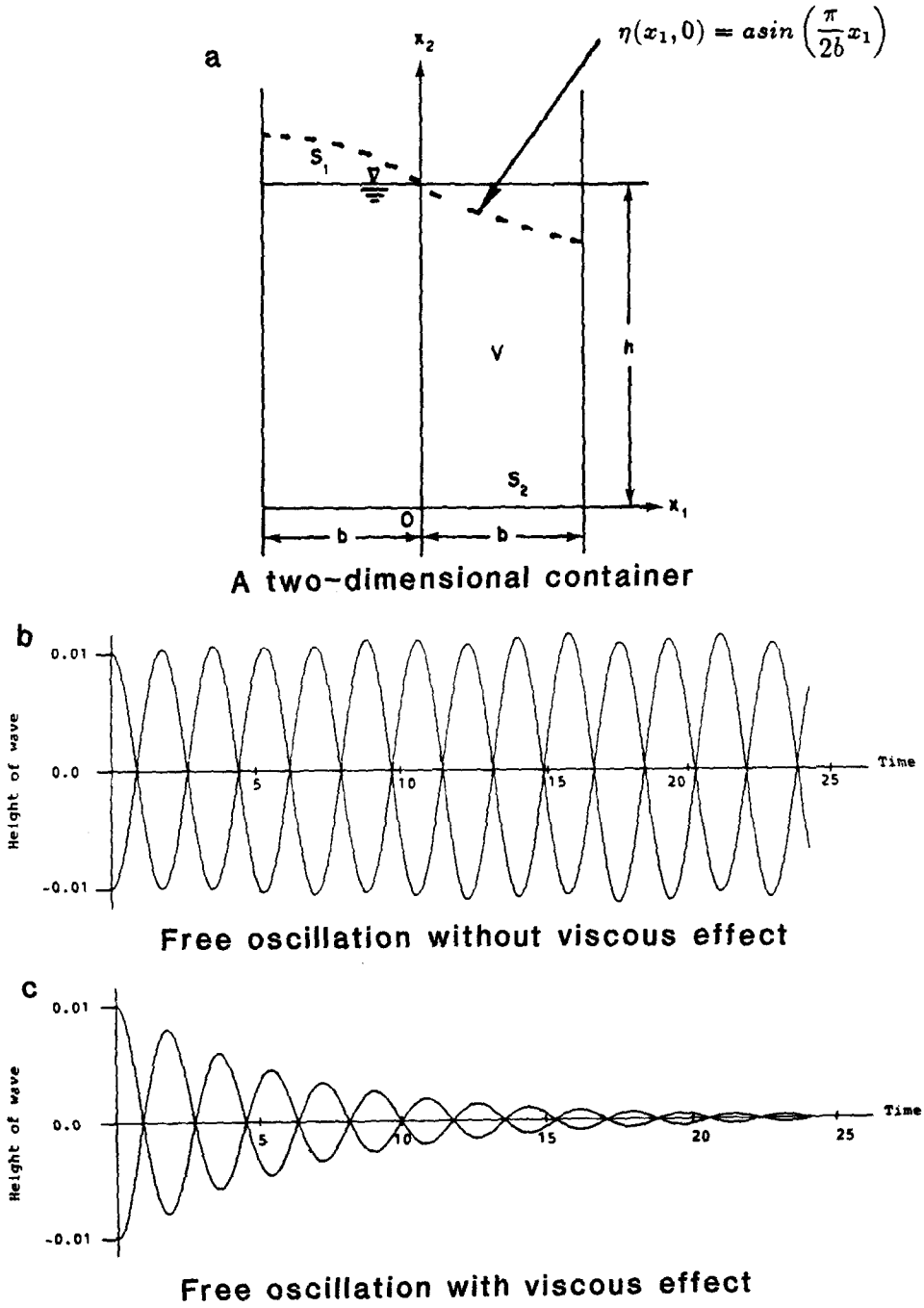

FIG. 3. Free oscillation: (a) a two-dimensional container; (b) free oscillation without viscous effect; (c) free oscillation with viscous effect.

A schematic view of the container used for the analysis is illustrated in Fig. 4. In the present example, the fluid initially occupies a region 4.8 units wide and 4.0 units high. A gravity acceleration of one unit acts downwards, and the amplitude of impulsive motion is assumed to be unity. The free slip boundary condition is specified on the solid boundary of the tank. The total number of nodal points and finite elements are 273 and 480, respectively. The computing conditions are as follows: $\Delta t = 0.005$, $\nu = 0.01$.

The calculation begins with a half-wave impulsive loading of the free surface as given in Eq. (55). Distortions in the flow domain can be seen from Fig. 5 for a

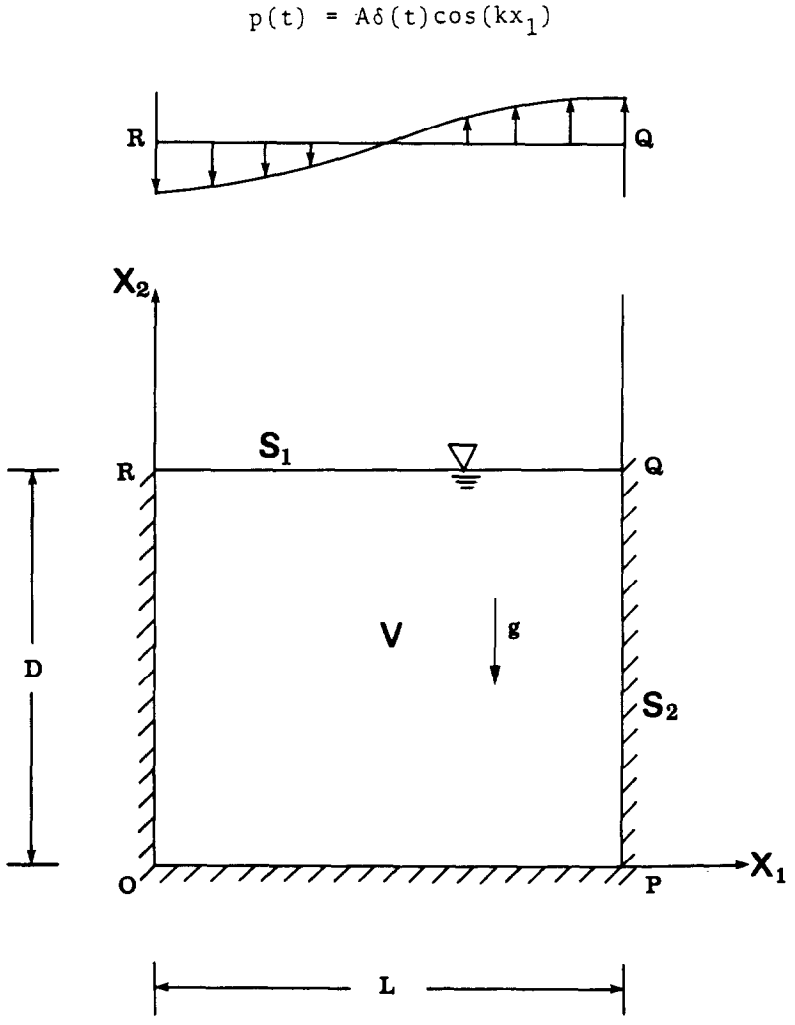

FIG. 4. Problem definition for sloshing dynamics.

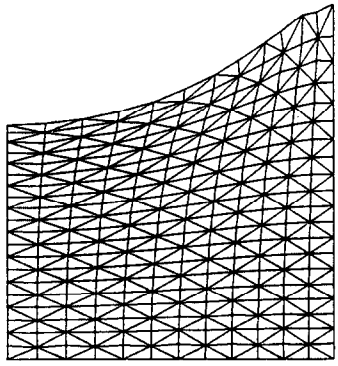

$t = 2$

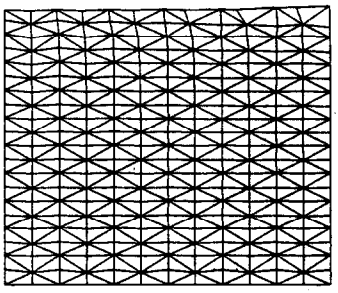

$t = 4$

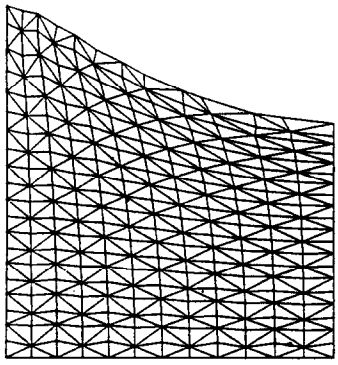

$t = 6$

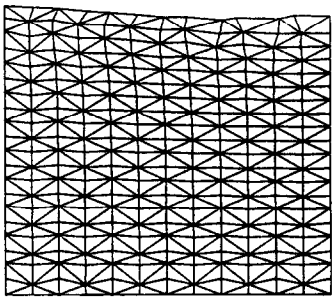

$t = 8$

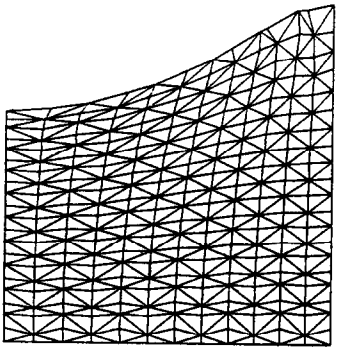

$t = 10$

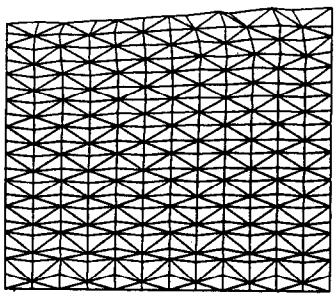

$t = 12$

FIG. 5. Computed mesh diagrams by Lagrangian method (the plots are times 2, 4, 6, 8, 10, 12).

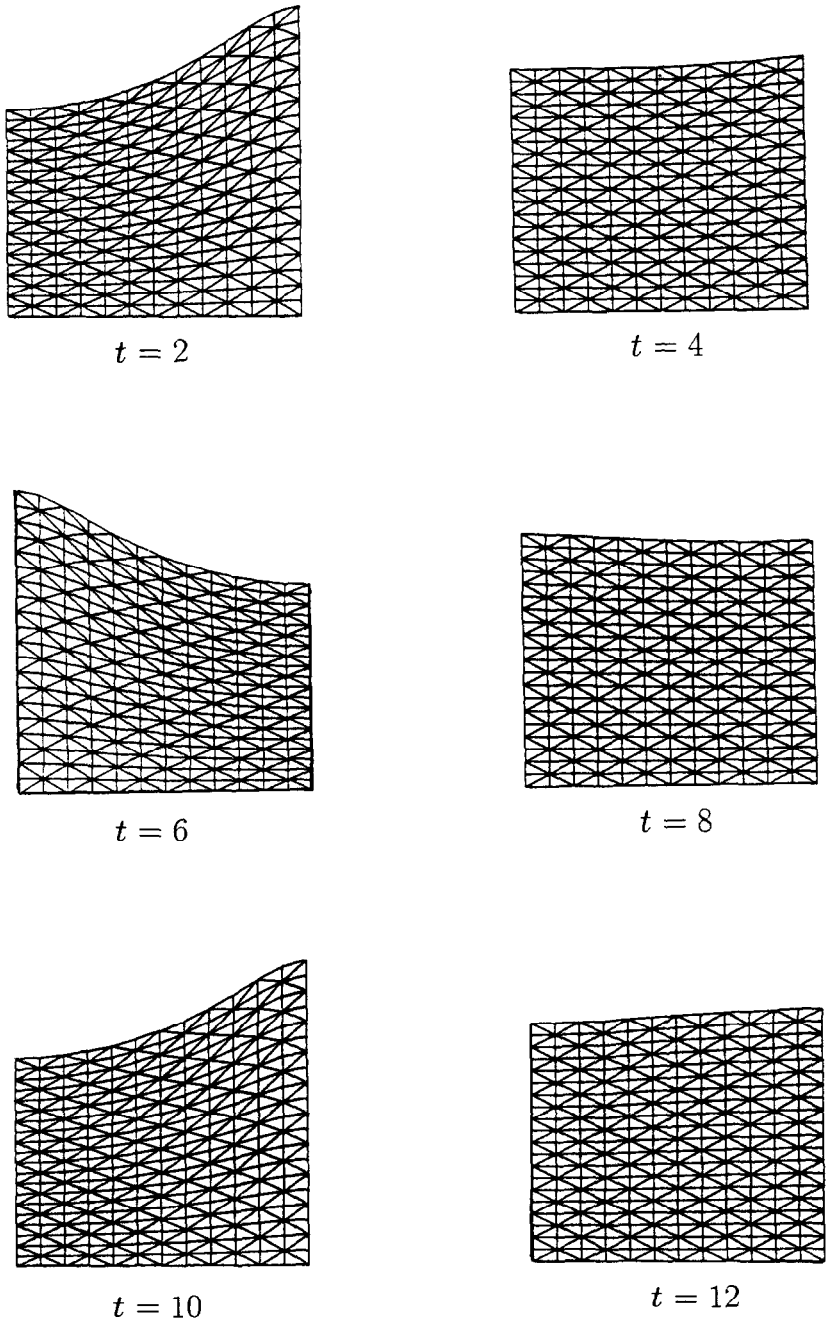

FIG. 6. Computed mesh diagrams by mixed Lagrangian–Eulerian method (the plots are times 2, 4, 6, 8, 10, 12).

highly nonlinear problem by the use of the Lagrangian calculation. Calculated results for this problem using mixed approach are shown in Figs. 6–8. In this calculation, the rezoning is performed at every 400 time levels, so that a desirable mesh configuration can be maintained. The amplitudes of the spikes and bubbles as functions of time through many complete periods of oscillation are shown in Fig. 9. One of the principal manifestations of non-linearity is seen in the enhanced amplitude of the spike side and the reduced amplitude of the bubble. The decreased frequency is indicated by shifts in both the time of the maximum amplitude and the times for a return to zero amplitude.

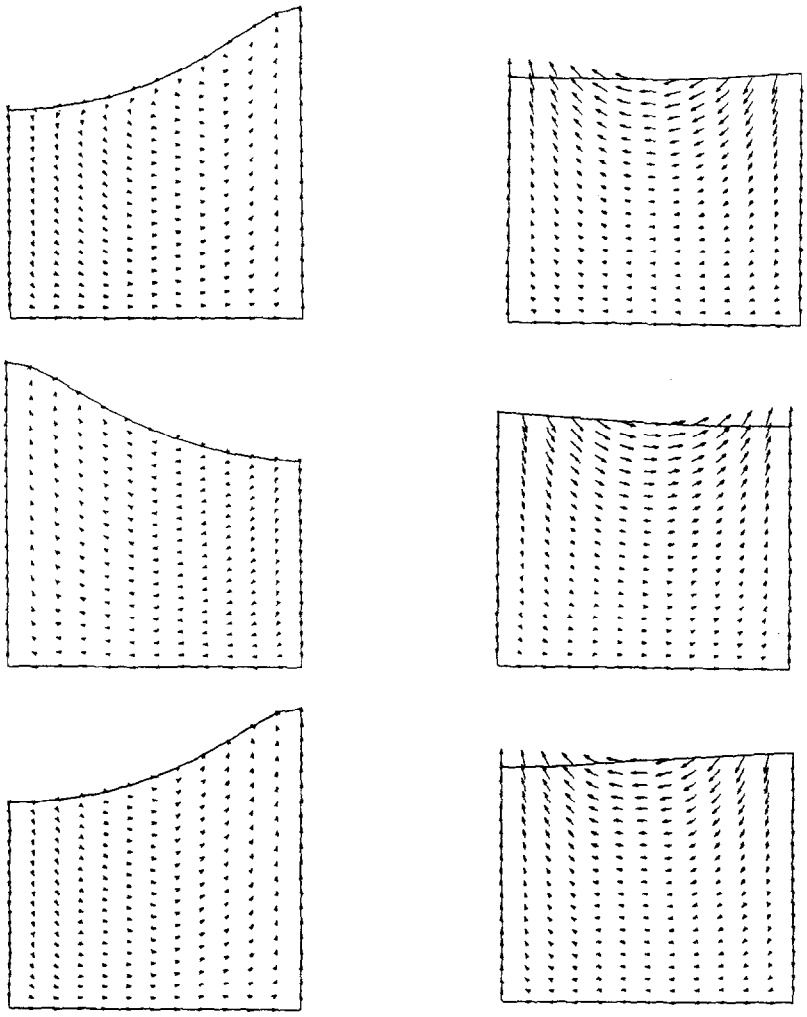

FIG. 7. Computed velocity vectors by mixed Lagrangian–Eulerian method (the plots are times 2, 4, 6, 8, 10, 12).

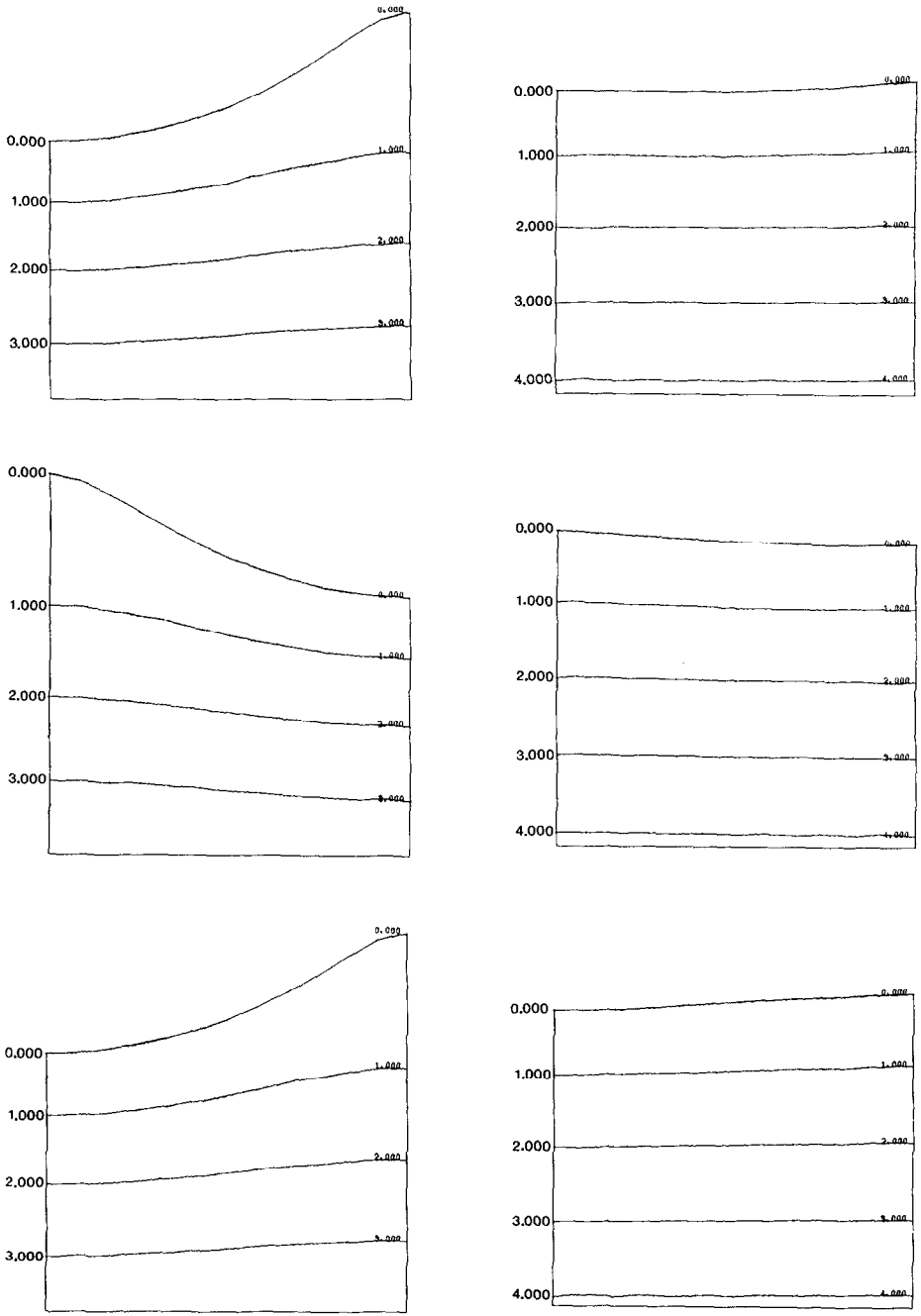

FIG. 8. Computed pressure distribution by mixed Lagrangian–Eulerian method (the plots are times 2, 4, 6, 8, 10, 12).

The computation of the non-linear oscillation in a tank with varying depths has also been carried out. A schematic view of the tank and the boundary conditions are shown in Fig. 10. The bottom width of the tank is 10.0 units and the depth is 10.0 units. A gravity acceleration of one unit acts downwards, and the amplitude of the impulsive motion is assumed to be 10.0 units. The calculation was performed with viscosity of 0.01 units. Time increment $\Delta t = 0.0025$ units was used and a stable calculation was obtained. Figure 11 shows a sequence of mesh configuration. In this calculation, the rezoning is performed at every 1000 time levels. From the results, it is obvious that the rezoning process makes a finer mesh where the speed of the fluid particle is high and a coarser mesh where the speed is low. The non-linear effects are also clearly shown in all these computed results by noting the movement of the nodal points in the whole region.

5.3. *Analysis of Solitary Wave Propagation*

The analysis for the propagation of a solitary wave is important for the design of breakwaters or sea walls and other offshore structures. The phenomenon of a solitary wave travelling in a rectangular channel of uniform depth was first reported by John Scott Russell in 1834. Russell defined the solitary wave as a single elevation above the surrounding undisturbed water level (neither followed nor preceded by any other elevation or depression of the surface) producing a definite transport in the direction of wave propagation only the wave travels without change of shape and with essentially constant velocity throughout the observable time of travel. Analytical studies for this problem have been carried out by many investigators [15–17]. Laitone's approximations of a solitary wave are frequently used for comparative study; in these approximations, velocity, pressure, and free surface elevation can be written in the forms

$$u_1 = \sqrt{gd}\,\frac{H}{d}\,\operatorname{sech}^2\left[\sqrt{\frac{3}{4}\frac{H}{d^3}}\,(x-ct)\right] \tag{56}$$

$$u_2 = \sqrt{3gd}\left(\frac{H}{d}\right)^{3/2}\left(\frac{y}{d}\right)\operatorname{sech}^2\left[\sqrt{\frac{3}{4}\frac{H}{d^3}}\,(x-ct)\right]\tanh\left[\sqrt{\frac{3}{4}\frac{H}{d^3}}\,(x-ct)\right] \tag{57}$$

$$\eta = d + H\,\operatorname{sech}^2\left[\sqrt{\frac{3}{4}\frac{H}{d^3}}\,(x-ct)\right] \tag{58}$$

$$p = \rho g(\eta - x_2) \tag{59}$$

$$c = \sqrt{gd\left(1+\frac{H}{d}\right)}, \tag{60}$$

in which H and d are the initial wave height and still water depth, respectively. In theory, Laitone's formula holds for an infinitely long channel only. Because the computations must be done in a finite domain and the fluid at a distance from the wave crest is essentially still, it is desirable to define a finite, practical length of

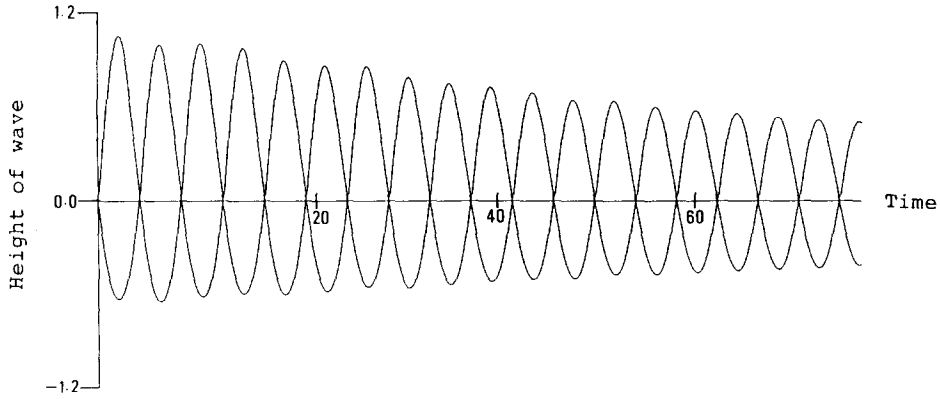

FIG. 9. Amplitudes of spike and bubble as functions of time for sloshing dynamics.

the solitary wave. The main consideration is that the two vertical walls which constitute the boundaries of the computation region should be far enough from the initial wave crest so that the motion of a solitary wave into the still water in front of a vertical wall can be closely approximated. For this purpose, the effective wavelength L was obtained by taking $L/2$ equal to the distance from the wave crest to the section where $\eta = 0.01\,H$ according to Laitone's formula; thus

$$\frac{L}{d} = 6.90\left(\frac{d}{H}\right)^{1/2}. \tag{61}$$

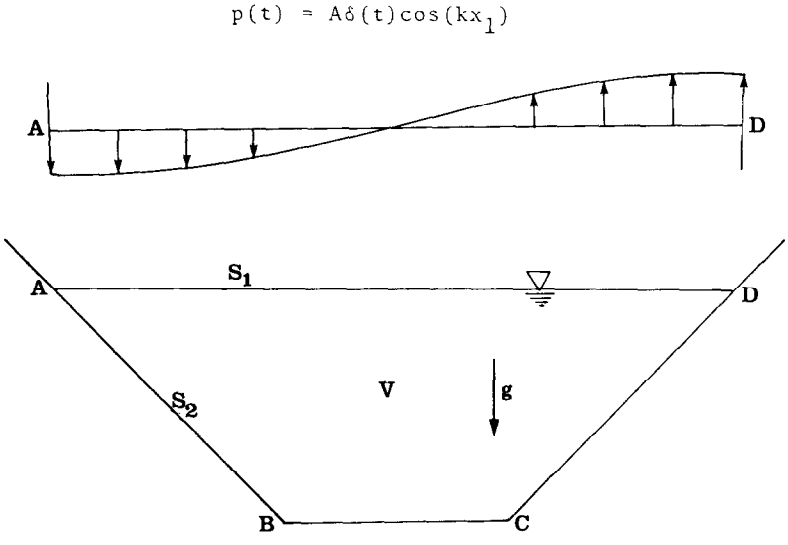

FIG. 10. Schematic and boundary conditions.

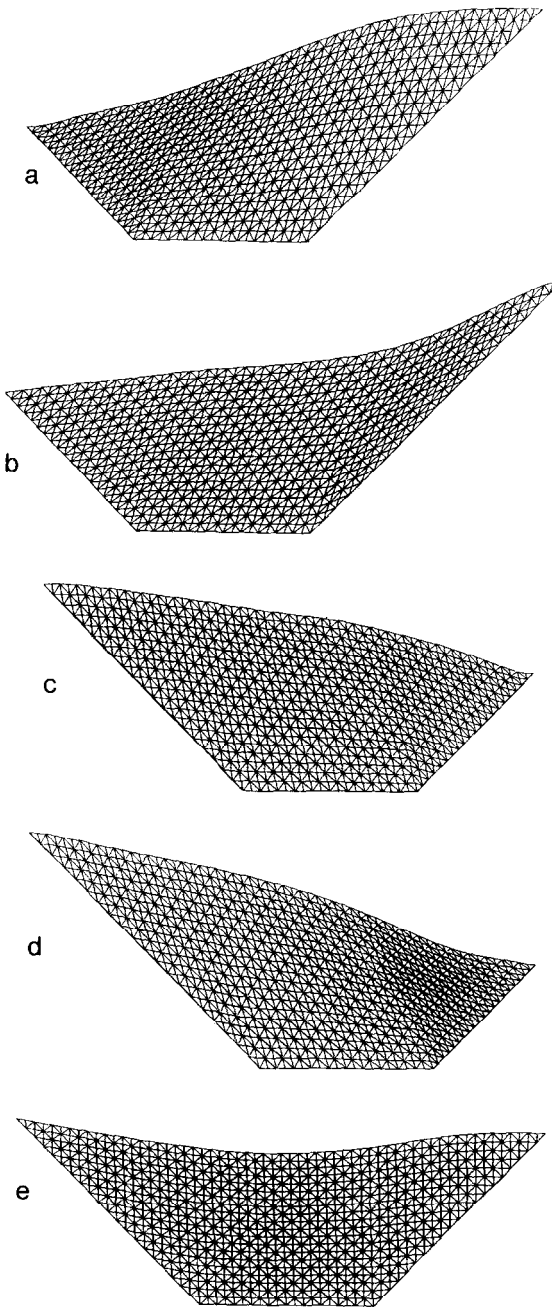

FIG. 11. *Computed results for nonlinear oscillation:* (a) *computed mesh diagram at time* $t = 5.0$; (b) computed mesh diagram at time $t = 10.0$; (c) computed mesh diagram at time $t = 15.0$; (d) computed mesh diagram at time $t = 20.0$; (e) computed mesh diagram at time $t = 25.0$.

With $H/d=0.2$, the value of $L/2$ is given by $8d$ by Eq. (61). Thus, the two vertical walls were located $16d$ away from the initial crest. The diagram is shown in Fig. 12, and the initial condition for this problem is illustrated in Fig. 13. The still water depth d is 10 units, the wave height H is 2.0 units and the horizontal length of the channel is $16d=160.0$ units. For computation, the density is assumed to be constant, the gravity acceleration is taken as $g=9.8$ units and the time increment $\Delta t=0.02$ time units is used. Starting from the initial condition, we can compute the behavior of the solitary wave. Computed wave profile, velocity, and pressure at elapsed times 7.7 units, 15.0 units, and 30.0 units are shown in Figs. 14–16. The time when the wave crest arrives at the right vertical wall from the center of the channel is 7.7 time units, which is close to Laitone's result.

The run-up height of a solitary wave on a vertical wall R can be obtained by Laitone's approximation:

$$\frac{R}{d}=2\left(\frac{H}{d}\right)+\frac{1}{2}\left(\frac{H}{d}\right)^2. \tag{62}$$

With $H/d=0.2$, R is 4.2 units in this computation, whereas our result is $R=4.48$ units. This clearly shows that the present method is not affected by any artificial damping effect. The pressure p is almost equal to hydrostatic pressure, and this result agrees reasonably well with practical behavior.

The computation of a solitary wave propagating through a channel with varying depths has also been carried out. A schematic of the channel and boundary conditions is shown in Fig. 17. The total number of finite elements and nodal points are 5760 and 3249, respectively. For the time interval, $\Delta t=0.02$ units was used and stable computation has been obtained. Computed velocity vectors and vertical velocity distributions at different time units are shown in Figs. 18 and 19. The solitary wave keeps its configuration through a constant depth. At time $t=30$, the

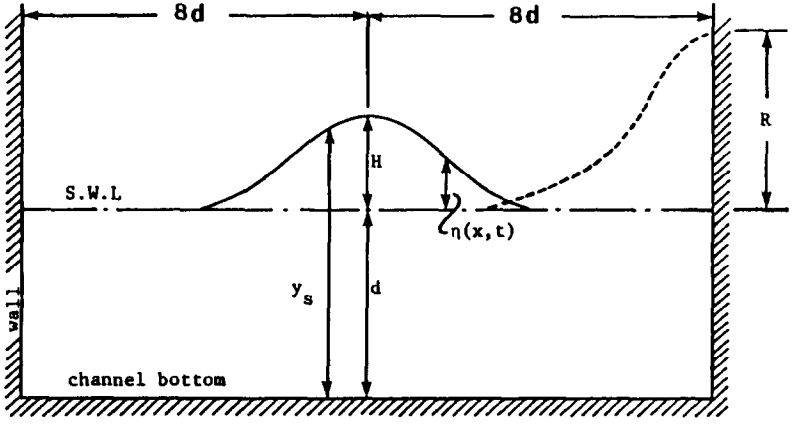

FIG. 12. Problem definition for solitary wave propagation.

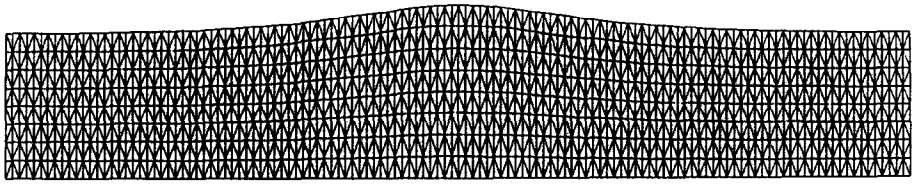

FIG. MESH

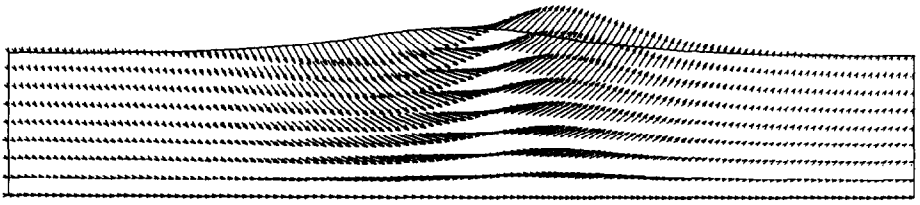

FIG. VELOCITY VECTOR

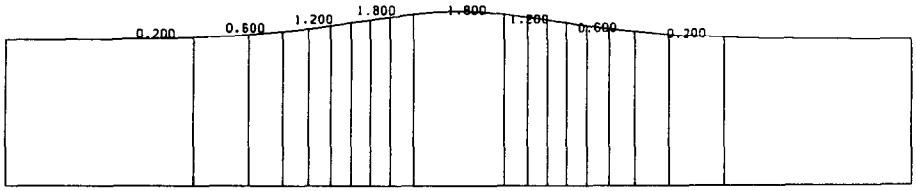

FIG. U DISTRIBUTION

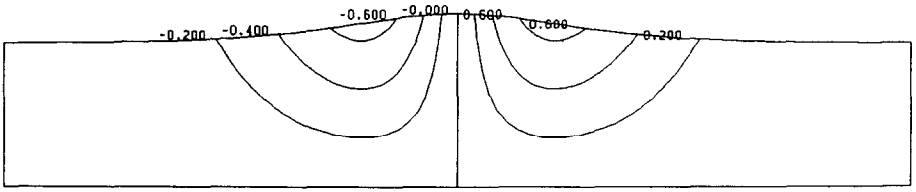

FIG. V DISTRIBUTION

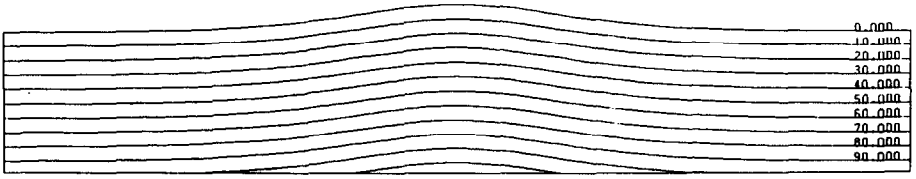

FIG. PRESSURE DISTRIBUTION

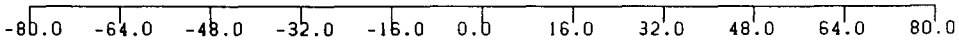

FIG. 13. Initial conditions.

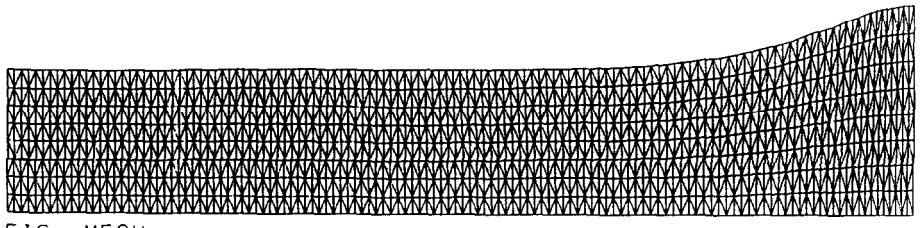

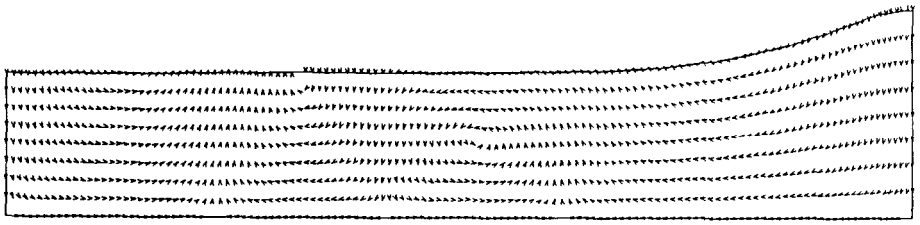

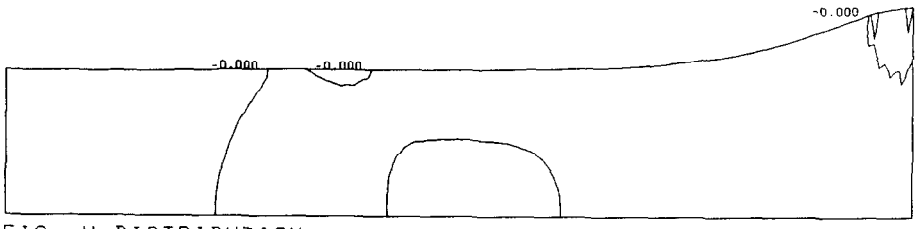

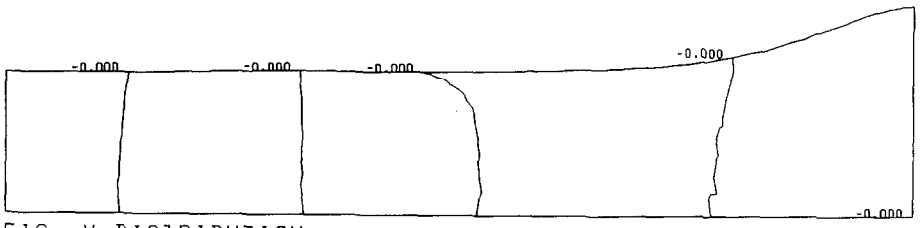

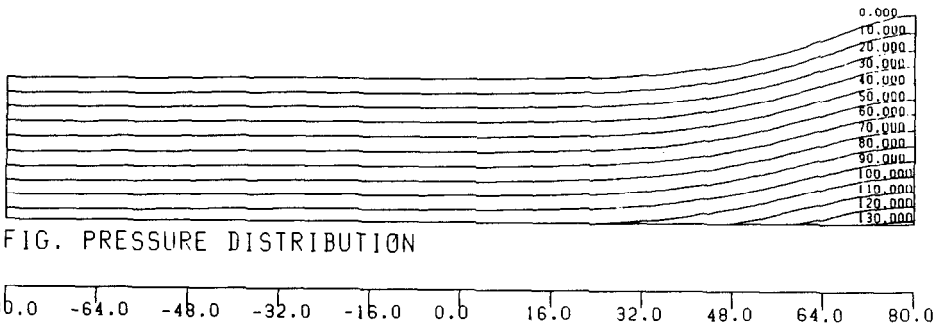

FIG. 14. Computed results at time $t = 7.7$.

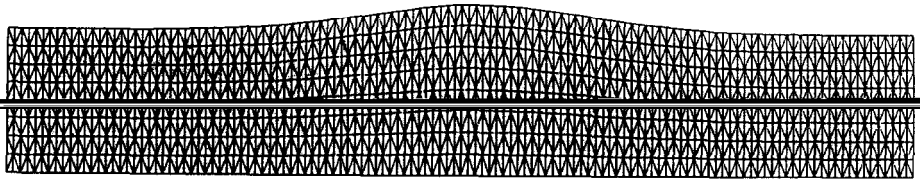

FIG. MESH

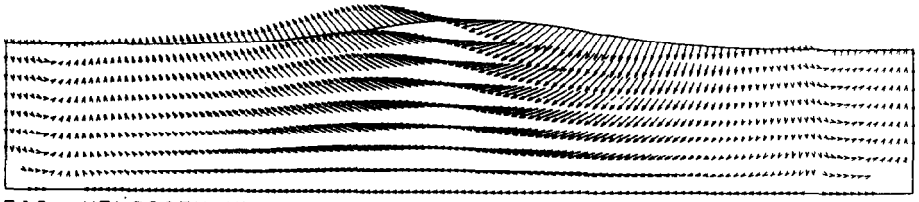

FIG. VELOCITY VECTOR

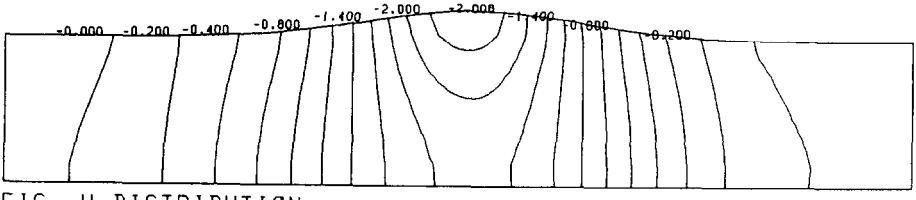

FIG. U DISTRIBUTION

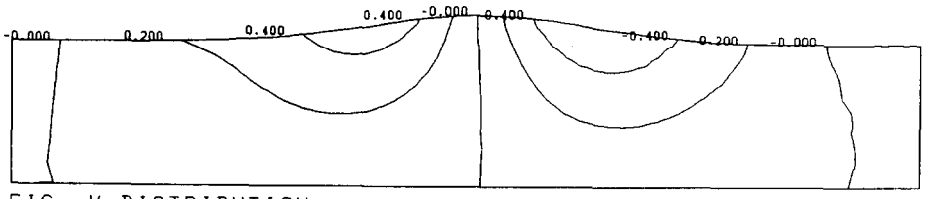

FIG. V DISTRIBUTION

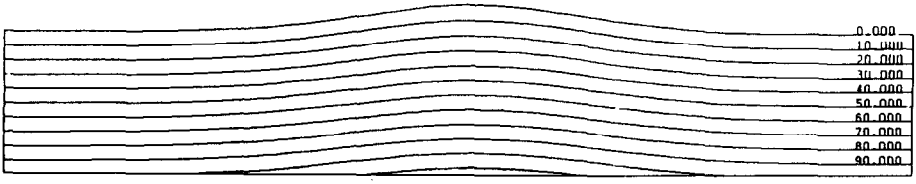

FIG. PRESSURE DISTRIBUTION

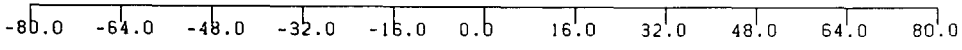

FIG. 15. Computed results at time $t = 15.0$.

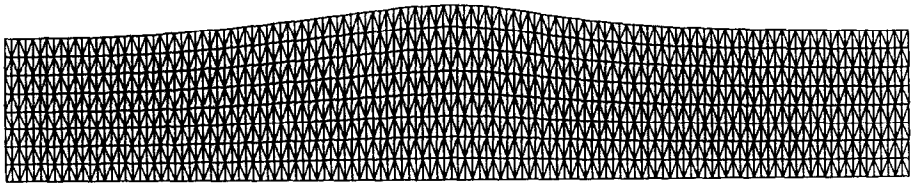

FIG. MESH

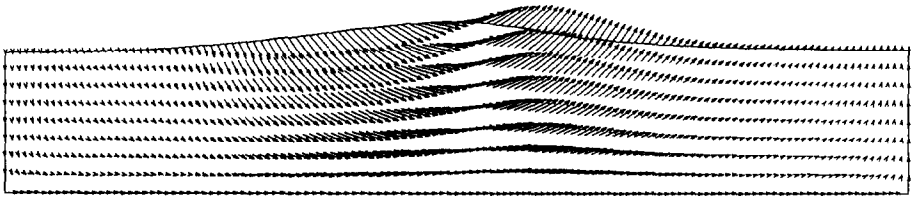

FIG. VELOCITY VECTOR

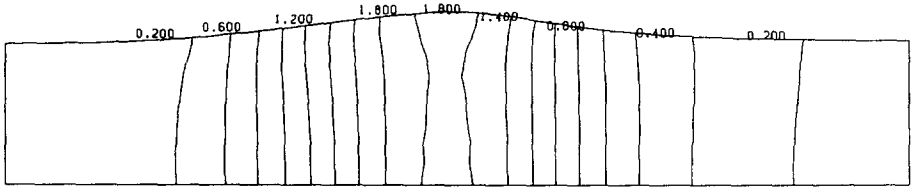

FIG. U DISTRIBUTION

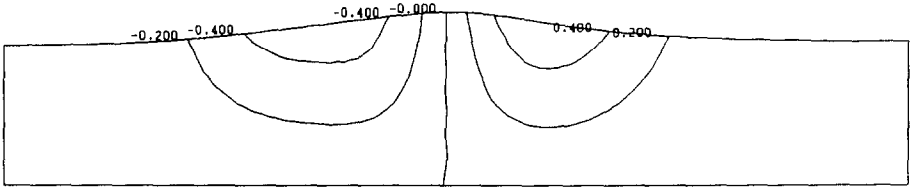

FIG. V DISTRIBUTION

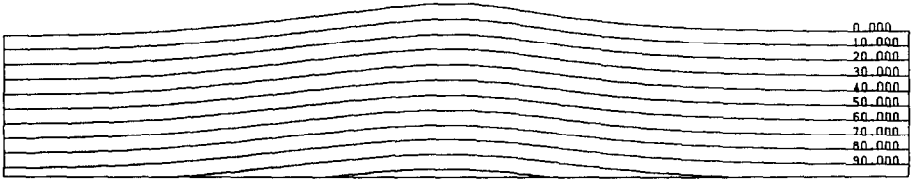

FIG. PRESSURE DISTRIBUTION

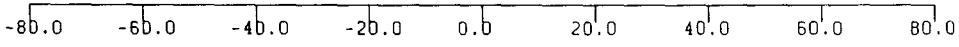

FIG. 16. Computed results at time $t = 30.0$.

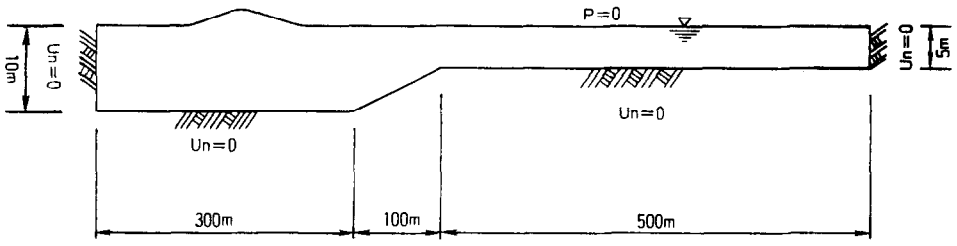

FIG. 17. Schematic and boundary conditions.

solitary wave arrives at the portion where the water depth changes, and the configuration of the wave separates into two waves. This behavior is more clearly shown at 40 time units. Because the velocity of the two waves are different from each other, the configurations become completely different, as shown in Fig. 18, which is the result at 70 time units. Thus, the successful application of the present approach to the run-up of a solitary wave indicates the possibility of employing the same technique to attack a wide variety of water wave problems. This extension will prove to be the most valuable in problems where analytic methods are difficult, if not possible.

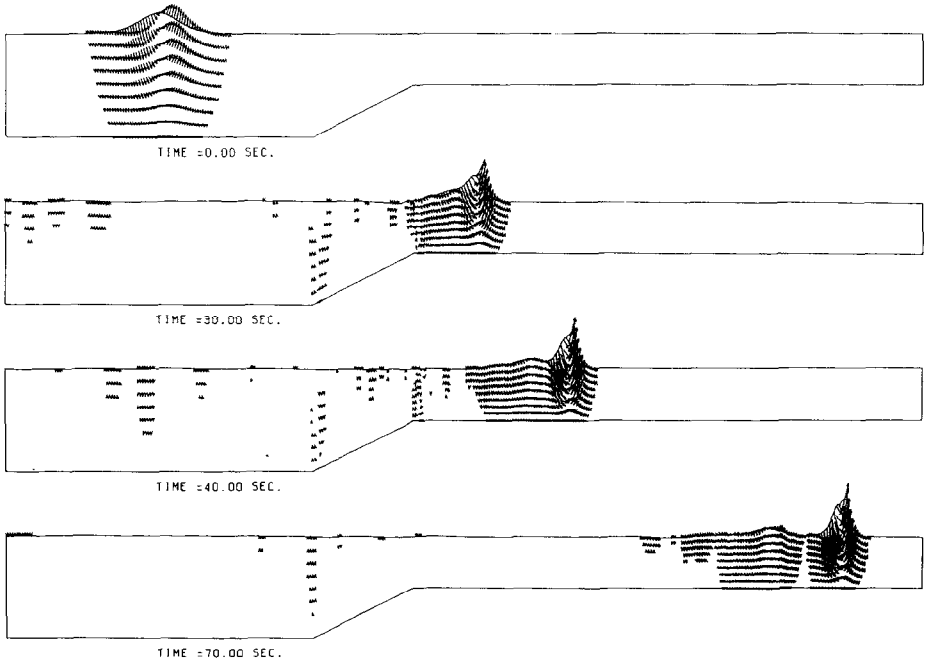

FIG. 18. Computed velocity vectors.

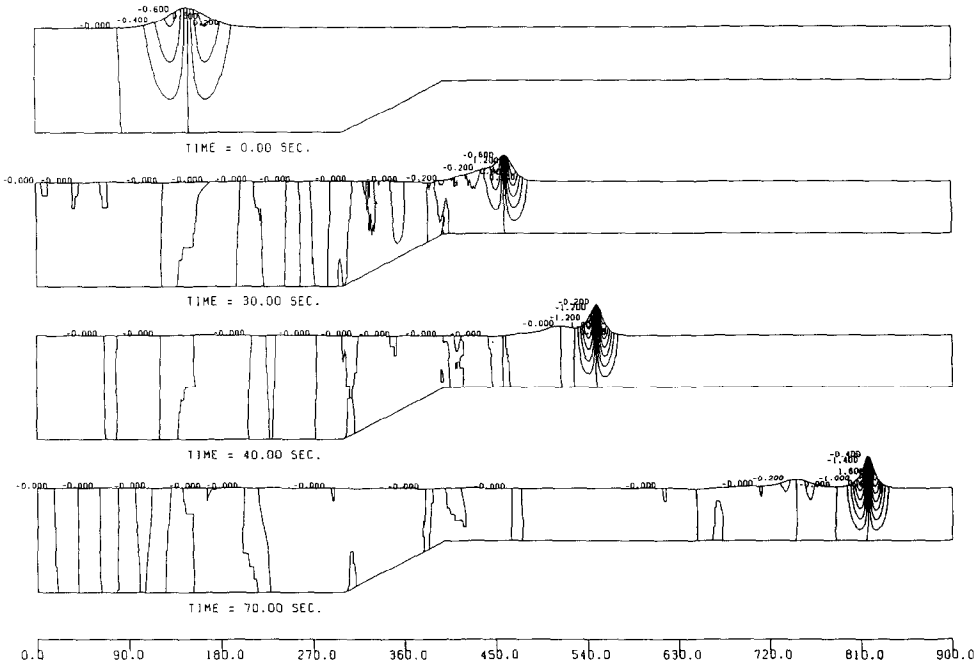

FIG. 19. Computed vertical velocity distributions.

5.4. *Generation and Propagation of Free Waves*

Wave tanks are used extensively in the investigation of water-wave phenomena and in model studies of proposed coastal structures. A vertical piston that oscillates horizontally near one end of the tank is quite commonly used to generate waves. The problem depicted in Fig. 20 is considered. The problem of motion that begins from rest at $t=0$ and the appropriate initial conditions are assumed as follows:

$$x_{\alpha 1}(t=0) = x_1^{(0)} \tag{63}$$

$$x_{\alpha 2}(t=0) = x_2^{(0)} \tag{64}$$

$$u_{\alpha i}(x_{\alpha i}, 0) = 0. \tag{65}$$

We suppose that the channel varies in depth and that it ends in a vertical impermeable wall. This implies that the following boundary conditions should hold:

$$u_{\alpha 2 \text{ at } x_{\alpha 2}=0} = 0 \tag{66}$$

$$u_{\alpha 1 \text{ at } x_{\alpha 1}=0} = 0. \tag{67}$$

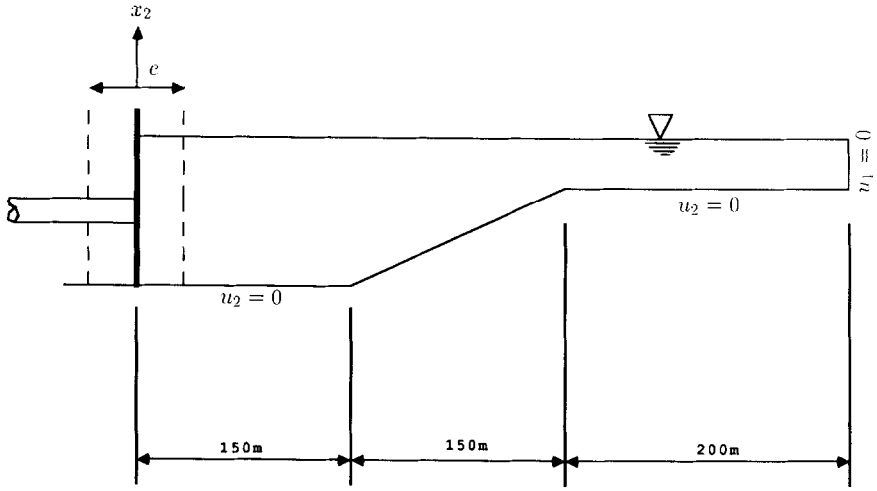

FIG. 20. Problem definition of a water tank and the wave maker.

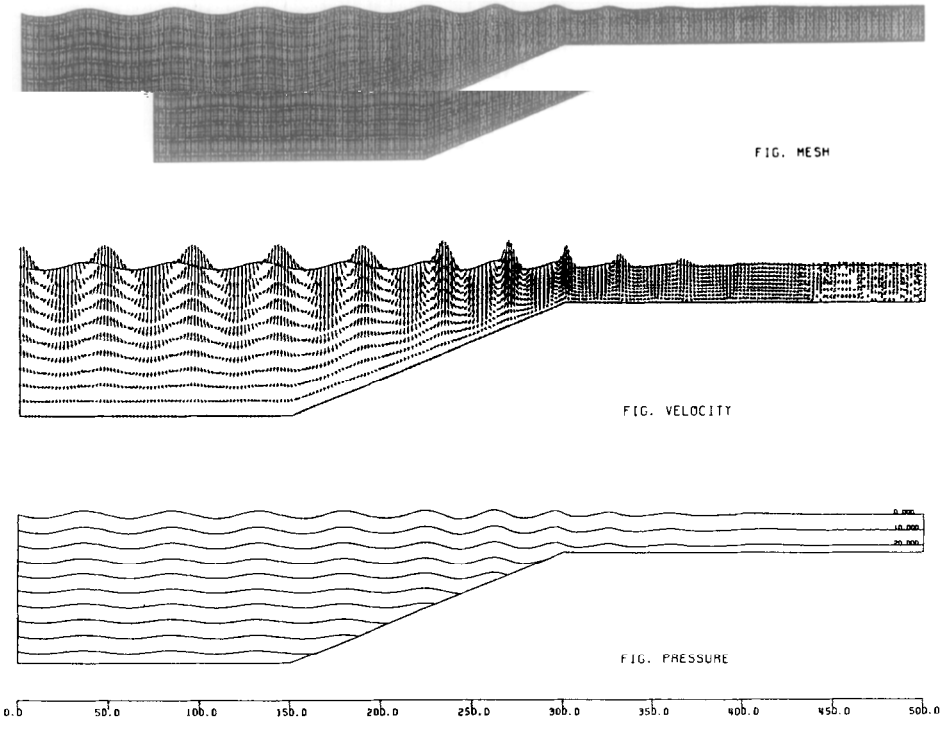

FIG. 21. Computed results at step = 3000 ($t = 60.0$).

Assuming that there is no leakage around the generator, we write the boundary condition at the generator as

$$\frac{d(x_{\alpha 1})}{dt} = u_g(t), \tag{68}$$

in which $x_{\alpha 1}(t)$ is the function that represents the displacement of the wave generator and is defined as

$$x_{\alpha 1}(t) = -e\cos(\sigma t), \tag{69}$$

where $u_g(t)$ corresponds to its velocity. Computed mesh configuration, velocity, and pressure distribution at time units 60 and 80 are shown in Figs. 21 and 22. In this calculation, the rezoning is performed at every 100 time levels. From these results it can be seen that the configuration of the free surface is in good agreement with the appearance observed in the experiments.

5.5. *Analysis of Density Flow*

There are a number of engineering problems that require the problem of a flow induced by the difference of fluid density to be solved. In recent years, much research based on the numerical analysis of such density flows has been presented.

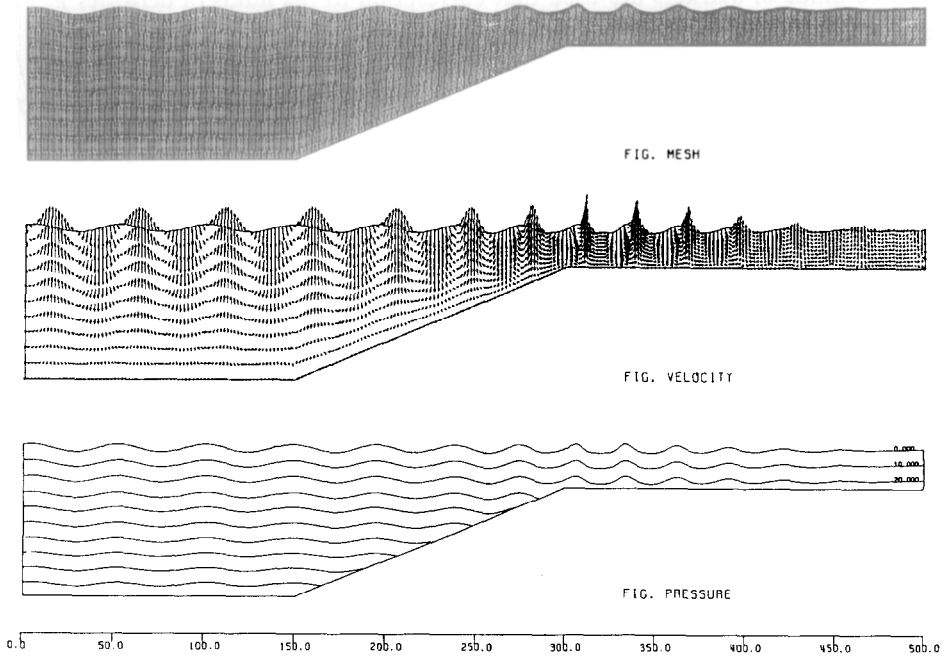

FIG. 22. Computed results at step = 4000 ($t = 80.0$).

One of the common types of analysis is referred to as the MAC method [18, 19], which uses many markers distributed in the flow field and moves them to pursue the loci of fluid particles. These analyses are mainly performed by the finite difference method. The basic idea can be successfully extended to the finite element analysis. The analysis presented in this paper is concerned with the mixing phenomena of two different fluids as shown in Fig. 23. The density distribution is not uniform throughout the flow field. However, the incompressibility condition and Boussinesq approximation are assumed to be valid because the time variation of density is not significant. The density distribution is computed from the manner in which the fluid particles are traced by markers attached to the fluid. The transient viscous incompressible flow can be expressed by the Navier–Stokes equations in the forms

$$\frac{\partial u_i}{\partial t} + u_j u_{i,j} = -\frac{1}{\rho_0} p_{,i} + \nu(u_{i,j} + u_{j,i})_{,j} + \frac{\rho}{\rho_0} f_i, \qquad \text{in } V, \tag{70}$$

$$u_{i,i} = 0, \qquad \text{in } V, \tag{71}$$

where ρ_0 represents the reference density.

In this paper, two phase-flow is analyzed in which the densities are ρ_1 and ρ_2. A number of markers are distributed in the flow field to distinguish fluid properties, and two kinds of markers are used that correspond to the fluids of densities ρ_1 and ρ_2. The position of a marker is moved according to

$$x_i^{n+1} = x_i^n + \Delta t u_i^n, \tag{72}$$

where x_i^n is the position of the marker at time point n. The density of fluid is computed at each finite element. Let the numbers of the markers at each finite element

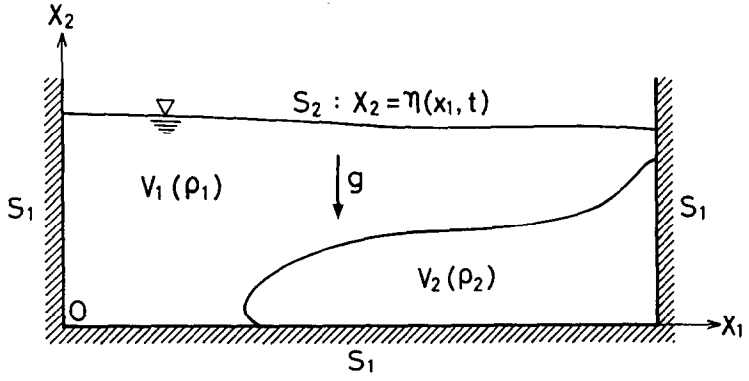

FIG. 23. Problem definition for density flow.

of the fluids with densities ρ_1 and ρ_2 be m_1 and m_2, respectively. The density of a finite element (i) can be computed as

$$\rho^{(i)} = \frac{m_1 \rho_1 + m_2 \rho_2}{m_1 + m_2}, \tag{73}$$

where $\rho^{(i)}$ is the density of the finite element (i). The reference density is computed by the weighted average finite elements at the initial stage,

$$\rho_0 = \frac{\sum_{i=1}^{M} \rho^{(i)} A^{(i)}}{\sum_{i=1}^{M} A^{(i)}}, \tag{74}$$

where $A^{(i)}$ is an area of finite element (i) and M is the total number of finite elements.

The schematic of the initial and boundary conditions is shown in Fig. 24. The boundary A-B-C-D is the wall on which

$$u_n = u_i \cdot n_i = 0 \qquad \text{on} \quad A-B-C-D \tag{75}$$

$$p_{,i} \cdot n_i = 0 \qquad \text{on} \quad A-B-C-D, \tag{76}$$

where u_n denotes the normal velocity. From Eqs. (76) and (39), it is found that

$$u_i^{n+1} \cdot n_i = \tilde{u}_i^{n+1} \cdot n_i \qquad \text{on} \quad A-B-C-D, \tag{77}$$

which corresponds to the fact that the normal velocity to the boundary is always equalized and is zero. The boundary A-D is the free surface on which

$$t_i = \left\{ -\frac{1}{\rho_0} p\delta_{ij} + \nu(u_{i,j} + u_{j,i}) \right\} \cdot n_j = 0. \tag{78}$$

As the initial condition, the barrier E-F is located to separate the fluids with densities ρ_1 and ρ_2, respectively. The computation begins by assuming that the barrier E-F is suddenly removed. A uniform mesh consisting of 341 nodal points

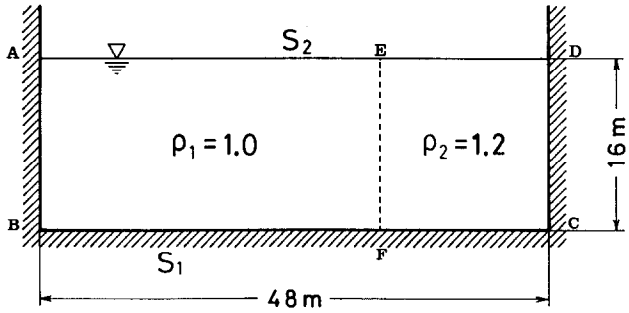

FIG. 24. Schematic view of initial and boundary conditions.

and 600 triangular finite elements is used. The computed velocity and density distributions at different time steps are represented in Fig. 25. The appearance of the mixing behavior can be seen clearly. (The heavier fluid lies under the lighter fluid.) The configuration of the free surface is also well suited to the appearance observed in conventional experiments.

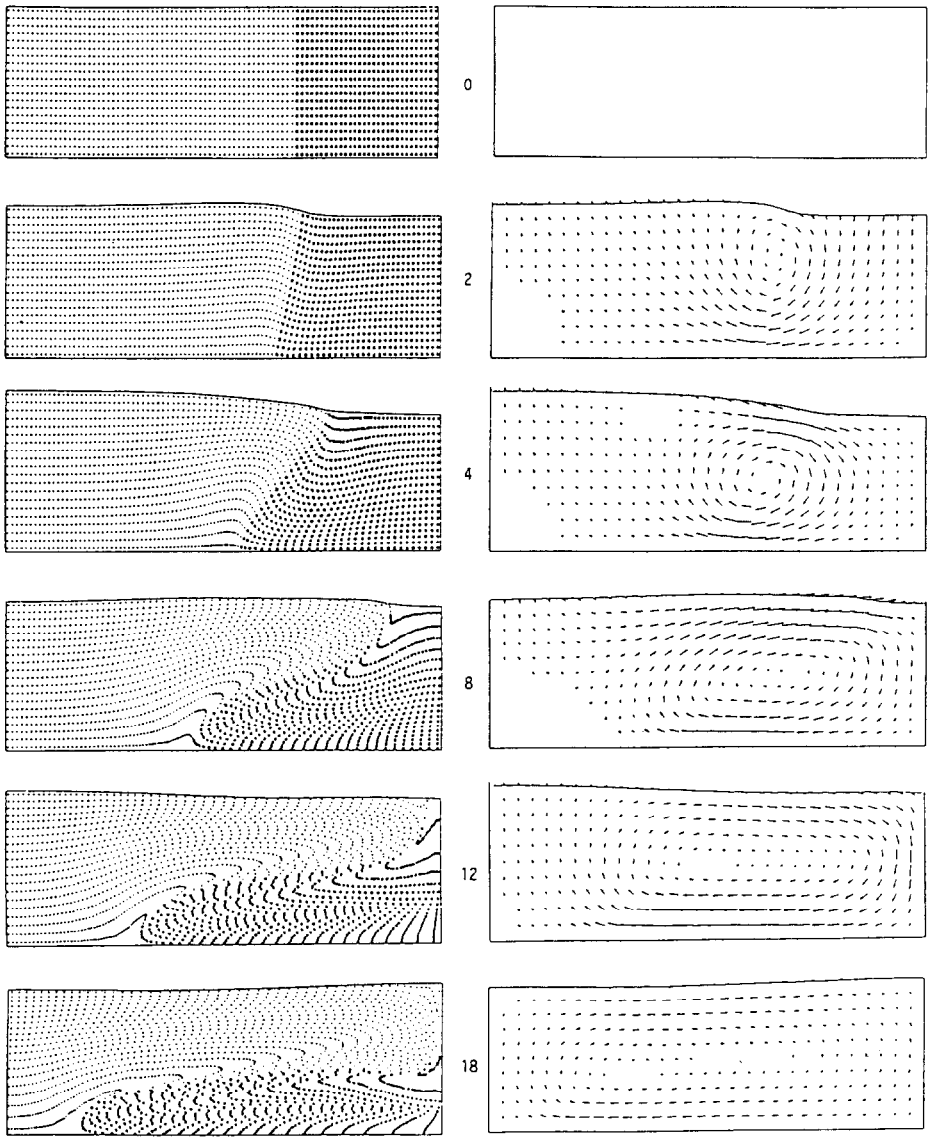

FIG. 25. Computed density distributions and velocity vectors (the plots are times 0, 2, 4, 8, 12, and 18).

6. Concluding Remarks

The following conclusions are drawn from the present study:

1. A new computing technique has been presented for calculating the transient dynamics of incompressible, viscous fluids with free surfaces. The examples demonstrate the method's flexibility in terms of geometry and boundary conditions, as well as its robustness in obtaining solutions to difficult problems.

2. The present work shows that the use of the Lagrangian finite element method for free surface viscous flow problems is elegant and that results of acceptable accuracy can be produced with a resonable computational expenditure. It also has the ability to calculate long-time solutions accurately without the benefit of artificial or numerical averaging. In general, the Lagrangian formulation is very useful for problems not involving large distortions, but requiring an accurate knowledge of free fluid boundaries.

3. The ALE technique is described in detail as it has been used to follow the free surface in an incompressible hydrodynamics code. The advantages of the ALE method include its ability to resolve arbitrary confining boundaries, to have variable zoning for purposes of obtaining an optimum resolution, and to be almost Lagrangian for improved accuracy in problems where fully Lagrangian calculations are not possible. Moreover, the ALE computing grid can always be rezoned to its original location, and it can be used for purely Eulerian calculations where boundaries can then be treated as rigid or as input and output walls.

4. The numerical procedure cited in this paper was demonstrated and verified through the solution of a mixing problem of two fluids with different densities. The method employs the idea the density variation can be pursued by using markers distributed in the flow field.

5. A very significant and worthwhile extension of the present work lies in the adaptive movement of the ALE mesh to minimize the finite element approximation errors. Since the user has the freedom to control the mesh, its movement for an optimal configuration is almost natural. As a closing statement, it can be said that because of the highly stable and convergent nature of this method, even for very large time steps, it will prove to be a useful tool in the solution not only of free boundary flow, but generally of time-dependent fluid dynamics problems.

Acknowledgments

The author would like to thank Professor M. Kawahara of Chuo University, Tokyo, Japan for his interest, encouragement, and many helpful discussions. The computations has been carried out using HITAC M680H computer of the University of Tokyo and Computer Aided Engineering Network System at the University of Michigan. The use of these computer facilities are also gratefully acknowledged.

REFERENCES

1. R. E. NICKELL, R. I. TANNER, AND B. CASWELL, *J. Fluid. Mech.* **65**, 189 (1974).
2. K. R. REDDY AND R. I. TANNER, *Comput. Fluids* **6**, 83 (1978)
3. F. M. ORR AND L. E. SCRIVEN, *J. Fluid. Mech.* **84**, 145 (1978).
4. W. J. SILLIMAN AND L. E. SCRIVEN, *J. Comput. Phys.* **34**, 287 (1980).
5. K. J. RUSCHAK, *Int. J. Num. Methods Eng.* **15**, 639 (1980).
6. H. S. KHESHGI AND L. E. SCRIVEN, *Finite Element Flow Analysis*, edited by T. Kawai (University of Tokyo Press, Tokyo, 1982), p. 113.
7. F. DUPRET, *Finite Element Flow Analysis*, edited by T. Kawai (University of Tokyo Press, Tokyo, 1982), p. 495.
8. L. C. WELLFORD AND T. H. GANABA, *Int. J. Num. Methods Eng.* **17**, 1201 (1981).
9. C. S. FREDERIKSEN AND A. M. WATTS, *J. Comput. Phys.* **39**, 282 (1981).
10. M. KAWAHARA AND T. MIWA, *Int. J. Num. Methods Eng.* **20**, 1193 (1984).
11. P. BACH AND O. HASSAGER, *J. Fluid. Mech.* **152**, 173 (1985).
12. B. RAMASWAMY, M. KAWAHARA, AND T. NAKAYAMA, *Int. J. Num. Methods Fluids* **6**, 659 (1986).
13. B. RAMASWAMY AND M. KAWAHARA, *Int. J. Num. Methods Fluids* **7**, 953 (1987).
14. C. W. HIRT, A. A. AMSDEN, AND J. L. COOK, *J. Comput. Phys.* **14**, 227 (1974).
15. E. V. LAITONE, *J. Fluid. Mech.* **9**, 430 (1960).
16. R. GRIMSHAW, *J. Fluid. Mech.* **46**, 611 (1971).
17. J. FENTON, *J. Fluid. Mech.* **53**, 257 (1972).
18. F. H. HARLOW AND J. E. WELCH, *Phys. Fluids* **8**, 2182 (1965).
19. A. A. AMSDEN AND F. H. HARLOW, *J. Comput. Phys.* **6**, 322 (1970).